ACS Catalysis

pubs.acs.org/acscatalysis
Research Article

Mechanistic Insights in the Catalytic Hydrogenation of CO_2 over Pt Nanoparticles in UiO-67 Metal−Organic Frameworks

Sri Harsha Pulumati, Dag Kristian Sannes, Christia R. Jabbour, Laurens D. B. Mandemaker, Bert M. Weckhuysen, Unni Olsbye,* Ainara Nova,* and Egill Skúlason*

Cite This: ACS Catal. 2024, 14, 382−394

ABSTRACT: Metal nanoparticles (NPs) encapsulated within Zr-based UiO-67 metal−organic frameworks (MOFs) have increased selectivity toward methanol in CO_2 reduction reactions. However, the reduction mechanism in these systems remains unclear. We built upon prior work examining the synergistic interaction between Pt nanoparticles and $Zr_6O_4(OH)_4$ clusters in UiO-67 and developed five distinct models representing the possible active sites in the Pt ⊂ MOF system. Density functional theory (DFT) calculations were employed to elucidate the CO_2 reduction mechanism toward methanol, methane, and CO formation. Our findings support previous evidence showing that the interface between the $Zr_6O_4(OH)_4$ cluster and platinum nanoparticles plays a crucial role in the activation of CO_2 to CO or formate intermediates and its further reduction to methane and methanol, respectively. Furthermore, we found different CO_2 hydrogenation mechanisms for interfaces involving Pt-flat terraces and Pt-edges. On Pt terraces and interfaces near Pt terraces, the reaction goes via CO, which can be desorbed as CO(g) or be further reduced to methane. On interfaces near Pt-edges, the reaction proceeds via formate and preferably forms methanol over methane. We designed experiments to validate our computational insights involving large and small Pt nanoparticles interacting with $Zr_6O_4(OH)_4$ clusters. These experiments showed that only CO and methanol were formed when smaller nanoparticles were present. Notably, methane formed with CO and methanol in the presence of larger nanoparticles, highlighting the need for flat platinum surfaces at the interfaces for methane formation. We could also associate the IR signals corresponding to CO and bidentate formate with platinum nanoparticles and $Zr_6O_4(OH)_4$ clusters, respectively. Theoretical models and experimental data provided us with insights into the complexity of the reaction mechanism and emphasized the significance of understanding both the individual components of the catalytic system and their interactions in enhancing catalytic activity.

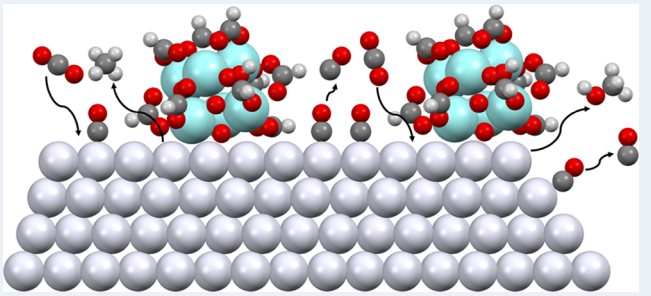

KEYWORDS: *UiO-67 metal−organic frameworks, $Zr_6O_4(OH)_4$ clusters, platinum nanoparticles, interface model, CO_2 hydrogenation, methanol, mechanism, catalysis, density functional theory calculations, experiments*

INTRODUCTION

Carbon dioxide (CO_2) is a primary greenhouse gas contributing to global warming and ocean acidification[1] yet also a potential carbon source for the postfossil chemical industry. The high stability of the CO_2 molecule renders its utilization energy-demanding.[2] Co-reactants such as H_2 have sufficient chemical energy to overcome the thermodynamic constraints of CO_2 conversion, and CO_2 hydrogenation over metal−supported catalysts is currently a hot research field.[3] As such, CO_2 capture and utilization is a promising pathway to reduce CO_2 emissions and produce fuels and high-value chemicals.

For CO_2 hydrogenation, the interface between the metal and support is essential.[4−6] Among the most studied catalyst materials for CO_2 hydrogenation are Cu supported on zirconia.[7−9] Cu-based catalysts supported on zirconia typically undergo CO_2 hydrogenation by generating stable formate and methoxy intermediates at zirconia sites close to the copper nanoparticles (NPs). The latter activates hydrogen and facilitates the reaction through spillover, providing a source of hydrogen. Interestingly, similar mechanisms were also observed using homogeneous catalysts, e.g., ruthenium[10] and iron[11] catalysts, bridging the gaps between catalysis fields.

Recent studies on CO_2 hydrogenation to methanol over metal-functionalized metal−organic frameworks (MOFs) have focused on unraveling the mechanism of methanol formation and have brought further evidence of the importance of

Received: July 24, 2023
Revised: November 22, 2023
Accepted: November 27, 2023
Published: December 19, 2023

https://doi.org/10.1021/acscatal.3c03401
ACS Catal. 2024, 14, 382−394

interaction between the NPs and the support.[12−14] Especially the UiO-type Zr-MOFs have received much attention due to their high thermal and chemical stability.[15] The inorganic cluster in UiO-type MOFs is the zirconium oxo cluster, $Zr_6O_4(OH)_4$. The cluster consists of six zirconium cations in an octahedral geometry, with each of the eight facets on the octahedron alternating, capped by either μ^3-O or μ^3-OH groups.[16] For the archetype UiO MOFs, UiO-66 and UiO-67, the clusters are connected by aromatic dicarboxylic acids, 1,4-benzenedicarboxylic acid and 4,4′-biphenyldicarboxylic acid, respectively.[17] The high stability of Zr-MOFs is attributed to the strong interaction between the high valent cation, Zr^{4+}, and the carboxylate groups of the linkers.[15] In ideal UiO-67, each zirconium cluster is coordinated to 12 4,4′-biphenyldicarboxylic acid linkers, although ideal coordination is rarely achieved.[18] When a monodentate capping agent replaces a linker, it is termed a missing linker defect.

Previously, three contributions have been published on UiO-67 functionalized with Pt NPs formed *in situ*.[12−14] In these studies, exceptional stability of the UiO-67-Pt material was observed, and the solid catalyst showed higher selectivity to methanol than the reference materials Pt/Al_2O_3, Pt/SiO_2, and Pt/C (carbon black).[12] However, the activity of the material is limited by the CO poisoning of the Pt NPs. *In situ* IR spectroscopy results suggested that methanol is formed via a formate species and is mechanistically separated from CO and methane, with the latter being a secondary product of CO. An inverse kinetic isotope effect (KIE) was observed for the methanol formation and, in combination with the presence of stable formate species, the anticipated rate-determining step (RDS) is the hydrogenation of the formate.[13] The methane formation rate also showed an inverse KIE upon H−D exchange, suggesting that a hydrogenation reaction is the RDS for methane formation. No KIE was observed for the formation of CO, indicating that the formation of CO does not involve breaking or making H−H, H−C, or H−O bonds in the RDS. Postsynthetic linker insertion resulted in a notable decrease in open zirconium sites, leading to a reduction of 60% in methanol and methane formation rates. In contrast, the formation rate of CO experienced only a minor decrease. These results suggest that open zirconium sites are essential for forming methanol and methane.[14] Overall, the findings from these experimental studies, supplemented by density functional theory (DFT) calculations, have facilitated the development of a viable mechanism for forming formate species. These contributions did not study the subsequent mechanisms for methanol and methane formation.

For UiO-type Zr-MOFs functionalized with Cu NPs, it was recently reported that CO_2 is strongly adsorbed in a tridentate mode at the interface of the copper NPs and the zirconium cluster.[19] However, no information about the mechanism of CO_2 reduction was provided by DFT calculations. X-ray photoelectron spectroscopy (XPS) analysis of similar Cu-MOFs showed that Zr in the proximity of Cu NPs is partly reduced, suggesting strong metal−support interactions.[20] Formate is formed after hydrogen spillover from the Cu NPs, and the RDS is generally considered the hydrogenation of surface formate species. Recently, Zhang et al. investigated the mechanism of CO_2 hydrogenation to methanol over single-atom sites in a Zn-functionalized MOF-808. The active site was found to be Zn^{2+}−O−Zr^{4+} sites, and formate was an intermediate of the mechanism, but interestingly, the RDS was the cleavage of the C−O bond in H_2CO−OH*.[21]

In this study, DFT calculations were used to unravel further mechanistic insight into CO, methane, and methanol formation over UiO-67 functionalized with Pt NPs. Furthermore, the effect of the Pt NP size on product selectivity was evaluated experimentally. Our calculations showed that the Pt NP size substantially influences product selectivity. A flat Pt surface interfacing with the Zr-cluster favors adsorbed CO formation, whereas an edged Pt surface favors adsorbed formate formation. We also show that formate hydrogenation is the RDS for methanol formation, consistent with the inverse KIE associated with a change in hybridization (from sp^2 to sp^3). The computational findings are supported by experimental results, where methane was only observed as a product when the catalyst contained large Pt NPs [3.5−12.5 nm] with a higher abundance of (111) microfacets.

COMPUTATIONAL DETAILS

In this study, DFT calculations were performed using the CP2K-8.1 package, where energy and forces were evaluated using the Gaussian and plane wave (GPW) method[22,23] as implemented in the Quickstep module[23] of CP2K. We utilized the PBE functional[24] with the DZVP-MOLOPT-SR-GTH basis set. The Goedecker, Teter, and Hutter (GTH) pseudopotentials[25,26] were used to represent core electrons, while double-ζ basis functions were used to represent valence electrons. Dispersion corrections are implemented using Grimme's DFT-D3 approach.[27,28] Gaussian basis functions were mapped using a multigrid of size 5, with a cutoff energy of 360 Ry and a relative cutoff of 60 Ry for determining the grid for Gaussian mapping. A tight convergence cutoff of 1×10^{-8} was used for all geometry optimizations and vibrational analysis.

Free energies are calculated at a temperature of 170 °C and pressure of 8 bar for all gas phase species and adsorbed and intermediate species on the active sites. In the case of adsorbed and intermediate species, a partial Hessian was computed involving only the atoms of the adsorbates for computational ease. Thermal corrections for the Gibbs free energies were computed from frequency calculations, using Shermo package,[29] where translational and rotational contributions were ignored for the adsorbed species, and only vibrational contribution was included. Energy barriers were calculated using the nudged elastic band (NEB) method,[30] starting each optimization with improved tangent NEB and switching to climbing image NEB[31] when the forces reached a threshold lower than 0.3 eV/Å, followed by a convergence criterion of 0.03 eV/Å for CI NEB.

Adsorption ΔG_a, desorption ΔG_d, and hydrogenation ΔG_h free energies are calculated as follows

$$\Delta G_a = G_{A*} - (G_{A(g)} + G_*)$$

$$\Delta G_d = (G_{A(g)} + G_*) - G_{A*}$$

$$\Delta G_h = G_{AH*} - \left(G_{A*} + \frac{1}{2}G_{H2}(g)\right)$$

where G_{A*} is the free energy of adsorbed species, $G_{A(g)}$ is the free energy of gas phase species, G_* is the free energy of the active site, G_{AH*} is the free energy of hydrogenated species, and $G_{H2(g)}$ is the free energy of the hydrogen molecule.

https://doi.org/10.1021/acscatal.3c03401
ACS Catal. 2024, 14, 382−394

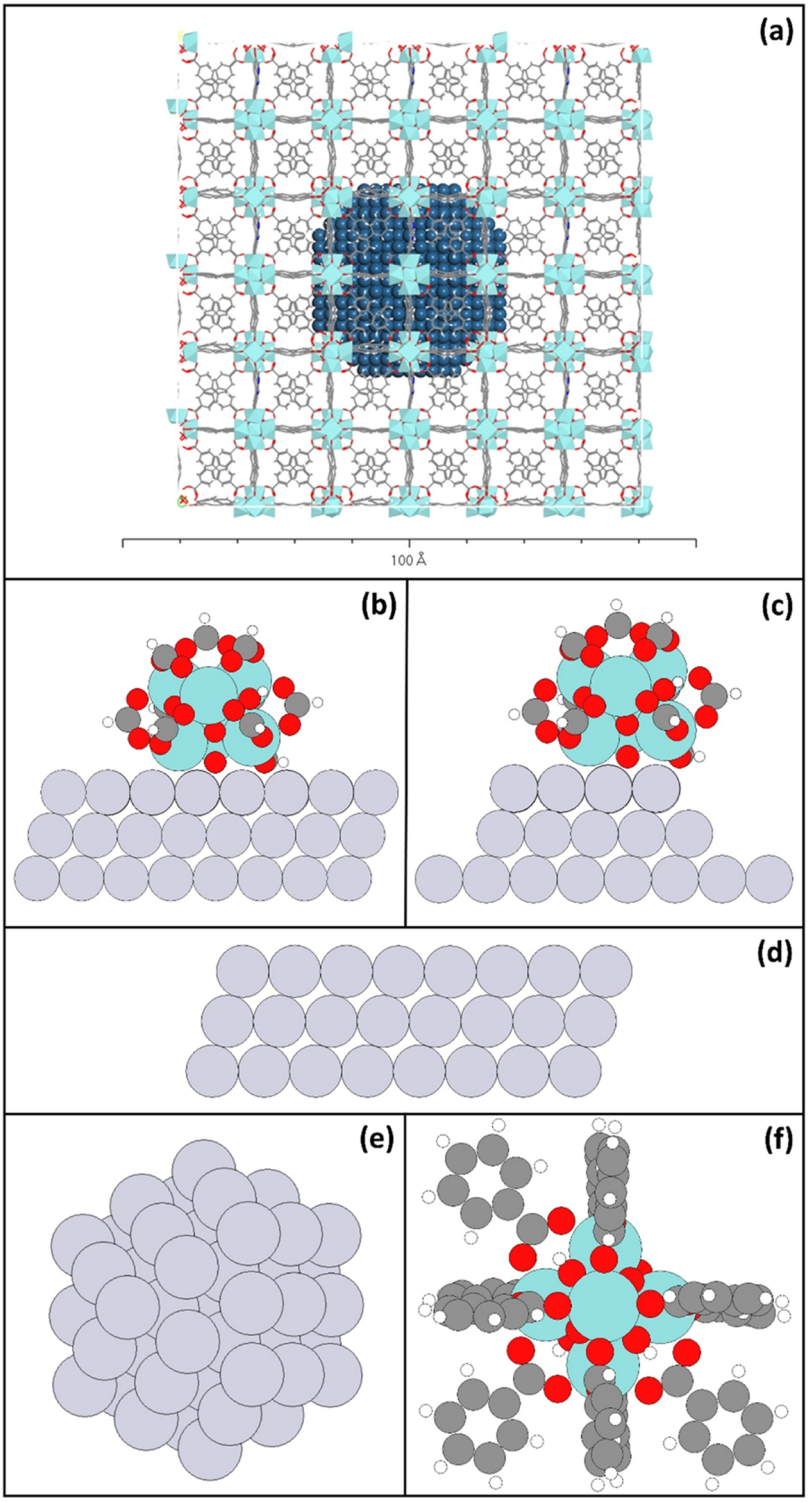

Figure 1. Model systems developed to study the CO_2 reduction reaction on a platinum-encapsulated UiO-67 MOF. (a) 1600-atom platinum nanoparticle encapsulated in UiO-67. (b) Defective zirconium cluster with linkers approximated as formate on top of a platinum (111) surface. (c) Defective zirconium cluster with linkers approximated as formate on top of an edge of a platinum surface. (d) Platinum (111) surface to simulate the flat surfaces of large nanoparticles. (e) 55-atom cuboctahedral nanoparticle of platinum to simulate the edges of the nanoparticle. (f) A defective zirconium cluster was created by removing one benzoate from a zirconium node bonded to 12 benzoate capping agents.

EXPERIMENTAL DETAILS

The starting material, further denoted as UiO-67, was purchased from ProfMOF A/S and is UiO-67 functionalized with 10% 2,2′-bipyridine-5,5′-dicarboxylic acid (BIPY). The chemical composition of UiO-67 was determined by using an already published procedure and was found to be $Zr_6O_4(OH)_4(BPDC)_{5.01}(BIPY)_{0.57}(benzoate)_{0.04}(formate)_{0.02}(H_2O/OH^-)_{0.79}$.[32] Using a previously published procedure, UiO-67 was further functionalized by incorporating platinum on the BIPY linkers.[12] Five grams of UiO-67 were submerged in 142 g

https://doi.org/10.1021/acscatal.3c03401
ACS Catal. 2024, 14, 382−394

of *N*,*N*-dimethylformamide (DMF), and 0.29 g of K_2PtCl_4 was added, resulting in a 1:2 ratio of platinum/BIPY (denoted UiO-67-$PtCl_2$). The mixture was heated at 100 °C for 24 h while stirring before filtration. The isolated material was dispersed twice in hot DMF and 5 times in ethanol for 5 min before drying at 120 °C for 24 h.

Subsequently, pyrolysis of the Pt-containing UiO-67 framework was conducted following two protocols, which produced materials with large and smaller Pt NPs, respectively. In the first protocol, UiO-67-$PtCl_2$ was first dried for 1 h at 200 °C under N_2 in a tubular oven before being modified by reducing the platinum in a continuous flow of H_2 at 350 °C for 4 h (sample denoted UiO-67-Pt). Then, the reduced sample was cooled and kept at 170 °C for 1 h and subsequently cooled from 170 °C to room temperature (RT) in argon before being subject to heat treatment at 550 °C in a continuous flow of N_2 for 5 h (sample denoted Pyr-UiO-67-large NPs). In the second protocol, UiO-67-$PtCl_2$ was first dried at 200 °C in N_2 for 1 h before being treated at 550 °C in N_2 for 5 h. The material was then cooled to RT before reduction in H_2 at 350 °C for 4 h (sample denoted Pyr-UiO-67-small NPs) and cooled and kept at 170 °C for 1 h before cooling to RT in argon. The Pt NPs in Pyr-UiO-67-large NPs have a most abundant size of 7.5 nm, while those in Pyr-UiO-67-small NPs have a most abundant size of 2.2 nm (Table S3).

Powder X-ray diffraction (PXRD) measurements were conducted on a Bruker D8-A25 instrument equipped with a Lynxeye detector and a Ge (111) Johanssen monochromator to select the Cu $K_{\alpha 1}$ radiation. Measurements were performed from 2θ = 2−50 with a step size and speed of 0.019° and 1 s, respectively. High-angle annular dark-field scanning transmission electron microscopy (HAADF−STEM) imaging was performed on a Talos F200X (FEI) microscope at 200 keV, equipped with an X-FEG electron source and a Super-X detector. Thermogravimetric analysis (TGA) results were obtained on a Netzsch STA 449 F3-Jupiter instrument. The samples were heated to 700 °C using a temperature ramp of 10 °C/min under a 100 mL/min flow of synthetic air using a crucible of Al_2O_3. Nitrogen adsorption isotherms were measured at −196 °C by using a BelSorp mini X instrument. The samples were pretreated at 200 °C for 2 h under vacuum using a Belprep vac II instrument. The specific surface areas were determined by using the Brunauer−Emmett−Teller (BET) theory. Scanning electron microscopy (SEM) images were recorded on an FEI Helios NanoLab G3 UC. Samples were loaded on aluminum stubs using a conductive carbon tape. The accelerating voltage was set to 2 kV, and the current was set to 0.10 nA. Microwave plasma atomic emission spectroscopy (MP-AES) was performed by using an Agilent 4100 MP-AES spectrometer. Prior to the measurements, 10 mg of the sample was dissolved overnight at 150 °C using 0.5 mL of sulfuric acid. H_2O_2 was then added to the hot solution to remove the carbon, followed by adding 0.5 mL of aqua regia and heating at 50 °C for two hours. ^{1}H nuclear magnetic resonance (^{1}H NMR) spectra of the digested MOF were obtained by using a Bruker AVIII HD 400 instrument. Sample characterization results are presented in the Experimental Details section of the Supporting Information.

The catalytic tests were performed using a fixed bed flow setup inside a commercial Microactivity Effi reactor (PID Eng & Tech). The setup consists of a stainless-steel reactor (I.D. 6 mm) coated with silicon, connected to an Agilent 8890 gas chromatogram (GC) equipped with one thermal conductivity detector (TCD) and two flame ionization detectors (FIDs). One of the FIDs was coupled to a methanizer to achieve lower detection limits of CO and CO_2. Before testing, the catalyst (0.2 g) was first reduced in 10% H_2 in inert for 4 h at 350 °C, using a 5 °C/min ramp with a total flow of 40 mL/min. The samples were tested using a 1/6/2 ratio of CO_2/H_2/inert (10% Kr in Ar) at 1−30 bar and 170 °C, with a contact time (τ) equal to 0.01 g_{cat} min/mL.

Strategy to Generate Computational Models and Reaction Pathways. *Computational Strategy*. The target system of investigation is UiO-67 MOF functionalized by Pt NPs *in situ* formed by sorption of $PtCl_2$ onto the BIPY linkers, followed by high-temperature reduction, as described in detail in prior publications[12−14] and in the Experimental Details section. An illustration of how a 2.2 nm Pt nanoparticle embedded in a UiO-67 MOF will look is presented in Figure 1(a). As represented in the figure, the Pt NPs supported on UiO-67 have a diameter larger than the diameter of the tetrahedral and octahedral cavities of the UiO-67 structure, which causes Zr-nodes to be displaced and decorate the surfaces and edges of the NP. Prior studies demonstrated the importance of the Pt NP−Zr-cluster interface as a CO_2 hydrogenation site, particularly the key role of open Zr sites for methanol formation.[13,14] However, the interaction of Pt NPs and MOF support and the missing linker defects that are inherent to the $Zr_6O_4(OH)_4$ clusters provide many possible active sites for CO_2 hydrogenation reaction; these include missing linker defect sites in MOFs, platinum terraces/edges on the nanoparticle, and the interfaces of displaced Zr-clusters and Pt NPs. To decrease the computational cost of this comprehensive study, we constructed simple models separating the identified active sites that could be studied independently. In the interface models, formate was used as a computational model for capping agents such as a linker, a linker fragment, a modulator, and formate generated from the CO_2 reduction.

To study the interface between Zr-clusters and platinum NPs, we needed two separate systems that simulate the interface between the Zr-cluster and the Pt NP terraces and edges. While creating these models, we found that the Zr-cluster with formate capping agents can be adsorbed on the Pt NP in two different orientations, one with three formates pointing toward the surface and one with four formates pointing toward the surface, as shown in Figure S17. These two orientations relate to the NP growth on the tetrahedral cage (3-formates) or octahedral cage (4-formates), as shown in Figure S18.

Zr-clusters with one, two, and three missing linker defects were also adsorbed on the Pt(111) surface. These calculations showed that the Zr-cluster with two defects adsorbed on Pt(111) in a 3-formate orientation has the lowest energy, considering adsorption and linker dissociation energies (Table S2 in the SI). This result and previous calculations suggesting that the NP growth occurs in the tetrahedral cage to maximize the Pt-linker interaction[13] made us select the 3-formate orientation for our study. Defects on the adsorbed Zr-cluster could result from initial missing linker defects or obtained during the reduction process.

Taking these considerations into account, the Zr-cluster with two removed formate capping agents adsorbed on a 3 atomic layers thick platinum (111) surface periodically repeated in an (8 × 8) supercell (Zr-cluster/Pt(111) model) was used to simulate the Zr-clusters situated on terraces of Pt NP. To simulate the interaction between the Zr-cluster and the edges

https://doi.org/10.1021/acscatal.3c03401
ACS Catal. 2024, 14, 382−394

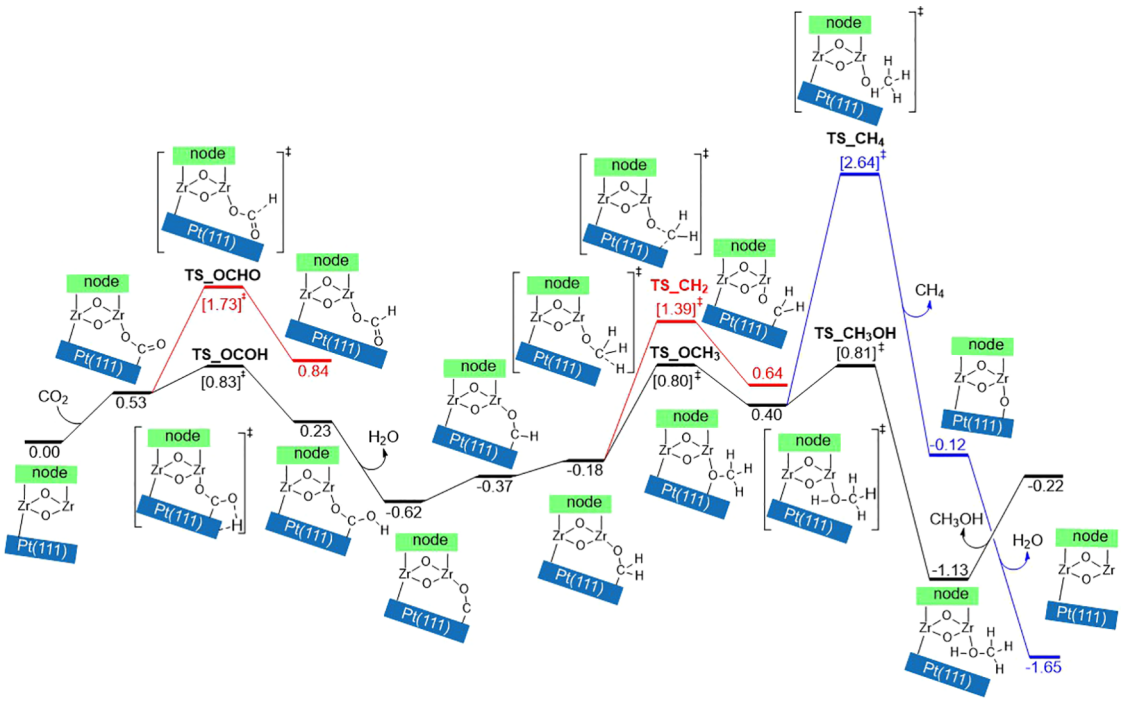

Figure 2. Calculated free energy (in eV) diagrams and energy barriers for CO_2 reduction reaction toward methane and methanol formation on Zr-cluster/Pt(111) model at 170 °C and 8 bar.

of the nanoparticle (Zr-cluster/Pt-edge model), we took the same model and removed Pt atoms from the first two layers, creating an edge-like feature. Our group has used a similar approach to study the hydrogen evolution reaction on Pt NPs[33] and N_2 dissociation barriers for Ru NPs.[34] This model was also repeated in an (8 × 8) supercell. These two interface systems are represented in Figure 1(b) and Figure 1(c).

The next set of active sites is on the flat surface of the platinum nanoparticles (i.e., microfacets), which was modeled by a Pt(111) slab of 3 atomic layers thickness periodically repeated in an (8 × 8) supercell, as shown in Figure 1(d). The close-packed (111) facet was chosen since it is the most abundant and lowest energy facet of a cuboctahedral NP. The choice for a three layers thick slab was made because, according to previous studies, it is a good compromise between accuracy and computational time.[35,36] In addition, similar CO hydrogenation energies were obtained using Pt slabs from three to six layers (Table S1). The bottom two layers of the Pt(111) slab and Zr-cluster/Pt(111) model and the bottom one layer for the Zr-cluster/Pt-edge models are constrained for computational ease. A cuboctahedral Pt_{55} nanoparticle with a diameter of approximately 11 Å (~1 nm), as shown in Figure 1(e), is used to represent the edges as well as (111) and (100) microfacets of the encapsulated nanoparticles in UiO-67. Finally, a defective Zr-cluster model was made, stripped down from UiO-67 to a single zirconium cluster with 12 benzoate capping agents from which one benzoate was removed to create an active site. The carbon atoms at the end of the linkers were constrained in all directions to prevent the cluster from deforming and simulate the cluster as part of the MOF framework, as shown in Figure 1(f).

We used the following approach to determine the reaction mechanism: after CO_2 adsorption on the active sites, hydrogen atoms were added to the oxygen or carbon atoms of CO_2 or to the μ^3-oxygen atoms of the clusters. The hydrogen atoms result from the homolytic cleavage of H_2(g) on the Pt surface, as proposed experimentally. Only the pathways with intermediates that are thermodynamically favorable were calculated further and are included in the original article or the SI. In selected cases, kinetic barriers were calculated to differentiate the formation of key products and intermediates.

Experimental Strategy. The experimental characterization of pristine (nonpyrolyzed) UiO-67-Pt, reported previously by us, revealed that Pt NPs had an average diameter of 3.6 nm, squared borders, and an irregular shape with well-defined terraces.[13] The size of those nanoparticles was significantly larger than the diameter of the tetrahedral (1.1 nm) and octahedral (1.7 nm)[37,38] cavities of the UiO-67 MOF, suggesting (and confirmed by DFT calculations) that the growth of Pt NPs is so energetically favorable that it may break the bond between the Zr-clusters and the carboxylate-functionalized linkers. The ensemble of results, including quantification of formate intermediates by SSITKA experiments,[13,14] suggested that Zr-clusters close to the Pt NPs were (partially or fully) detached from the lattice and were decorating the Pt NPs.

While the effect of linker defects and open Zr sites in UiO-67 was experimentally investigated in prior contributions, the effect of Pt NP size was yet unexplored. To this end, we followed a novel strategy in this contribution, i.e., to produce Pt NPs with substantially different particle sizes by pyrolyzing the UiO-67 material after $PtCl_2$ sorption, using two different experimental protocols (see the Experimental Details section). Using these protocols, the produced materials have the most abundant diameters of the Pt NPs of 2.2 nm (Pyr-UiO-67-small NPs) and 7.5 nm (Pyr-UiO-67-large NPs). Characterization data for the two materials are presented in Table S3 and Figure S25.

https://doi.org/10.1021/acscatal.3c03401
ACS Catal. 2024, 14, 382−394

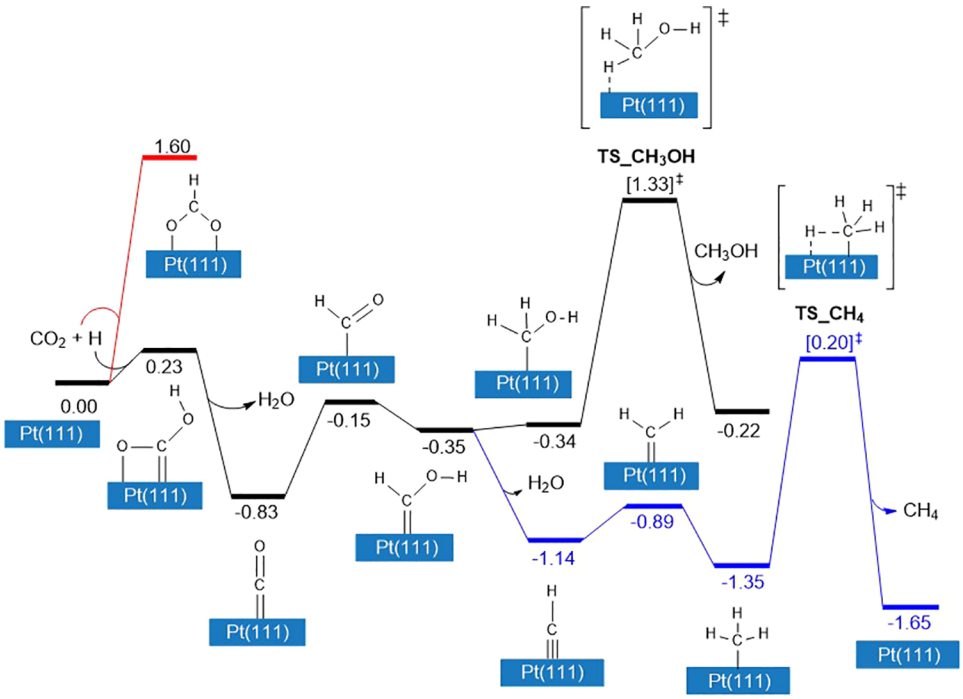

Figure 3. Calculated free energy (in eV) diagrams and energy barriers for CO_2 reduction reaction toward methane and methanol formation on the Pt(111) surface at 170 °C and 8 bar.

RESULTS

$Zr_6O_4(OH)_4$ Cluster on a Pt(111) Surface (Zr-Cluster/Pt(111) Model). The lowest free energy pathways for the hydrogenation of CO_2 to methanol and methane with the Zr-cluster/Pt(111) model are represented in Figure 2. First, the adsorption of a gas phase CO_2 molecule onto the defect site at the interface is endergonic (0.53 eV), followed by an exergonic hydrogenation step of CO_2 to *OCOH (−0.3 eV). This pathway is thermodynamically and kinetically (Figure S1) more favorable than the hydrogenation of C to form formate, which is endergonic (*OCHO, 0.3 eV). The hydrogenation of *OCOH is also exergonic and yields desorbed $H_2O(g)$ and *CO at the interface, with *CO being the lowest free energy intermediate (Figure 2). Next, *CO undergoes three endergonic hydrogenation steps, forming *OCH_3 through *OCH and *OCH_2.

The *OCH_3 intermediate at the interface can be hydrogenated to form methanol or methane, depending on the hydrogenation of C or O, respectively. While both reaction steps are exergonic, the energy barrier for hydrogenation of *OCH_3 to form methane (2.24 eV) is much higher than for methanol formation (0.41 eV, Figure 2). In addition, methane desorbs to the gas phase upon hydrogenation, while methanol is adsorbed on the interface (Figures S2 and S3 for minimum energy pathways). From the free energy landscape and kinetic barriers in Figure 2, methane's overall activation free energy is 3.26 eV, and methanol is 1.43 eV. These energies are calculated as the difference between the transition state to form and desorb methane and methanol and the energy of CO*, which is the lowest reaction intermediate.

As the kinetic barrier for hydrogenation of *OCH_3 to form methane was unusually high, we attempted to break the O−C bond and migrate CH_3 onto the Pt(111) surface but were unsuccessful. During NEB optimizations, we noticed that CH_3 dissociates to CH_2 and H that adsorb on the Pt, as shown in Figure S12 of the SI. This prompted us to consider the cleavage of the O−C bond in the *OCH_2 intermediate to form the *CH_2 intermediate on the Pt(111) surface. This step has an energy barrier of 1.57 eV (Figures 2 and S10). However, the barrier and free energy state of the *CH_2 intermediate on the Pt(111) surface is higher than the hydrogenation of *OCH_2 to form *OCH_3 (Figure S11), the mechanism proceeds toward methanol, as shown in Figure 2.

From the free energy diagram, the preferred mechanism for CO_2 hydrogenation on the Zr-cluster/Pt(111) model goes via a CO intermediate and prefers methanol formation instead of methane. These results differ from the experimental observations for the CO_2 hydrogenation reaction on the UiO-67-Pt system from our previous study,[13] where the kinetic studies with H_2 and D_2 suggested that formate is a reaction intermediate for forming methanol. This absence of a formate intermediate suggests that the Zr-cluster/Pt(111) model may not represent the most abundant sites for methanol formation in the experimental system.

From the free energy diagram in Figure 2, methane formation is not favorable on the Zr-cluster/Pt(111) interface due to a very high activation energy. However, the CO intermediate can migrate from the interface to the Pt(111) slab representing the (111) microfacet of the Pt NP. The free energy for this migration step is 0.12 eV, after which the hydrogenation reaction can continue on the Pt(111) surface, which is discussed below.

Platinum (111) Surface. While studying the hydrogenation reaction on a Pt(111) surface, we found that $CO_2(g)$ did not adsorb onto the platinum surface. Therefore, the hydrogenation reaction must start with a concerted step of CO_2 hydrogenation and adsorption to form *COOH, which may involve a substantial kinetic barrier and be a slow process. However, as explained above, the CO_2 activation/adsorption and formation of the *CO intermediate may occur at the Zr-

https://doi.org/10.1021/acscatal.3c03401
ACS Catal. 2024, 14, 382−394

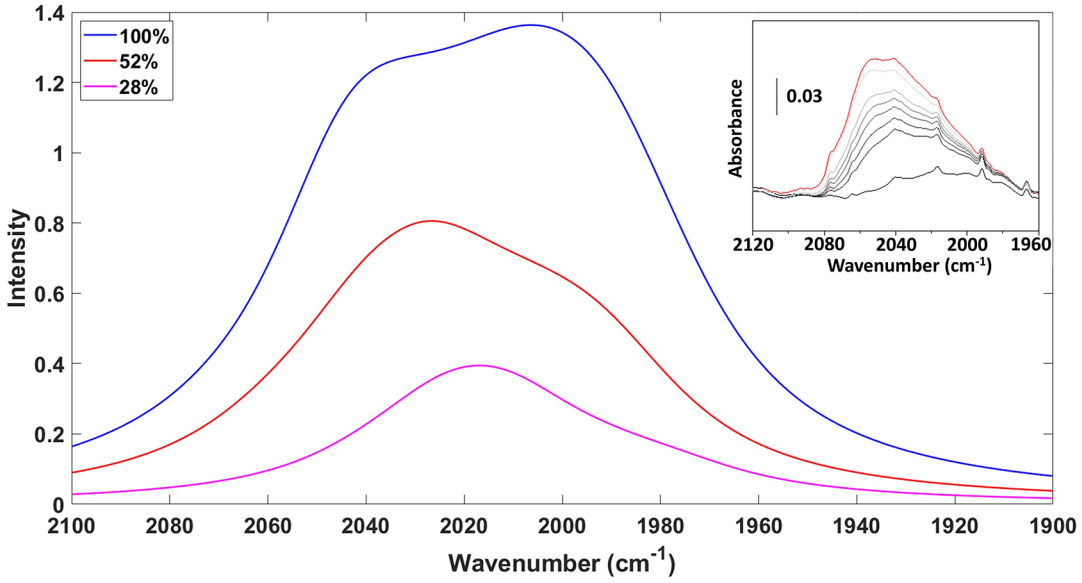

Figure 4. Simulated IR spectroscopy plot of CO adsorbed on the Pt_{55} nanoparticle at varying surface CO coverage (100, 52, and 28%). The inset image shows experimental FT-IR spectra of CO linearly adsorbed on the metal nanoparticles.

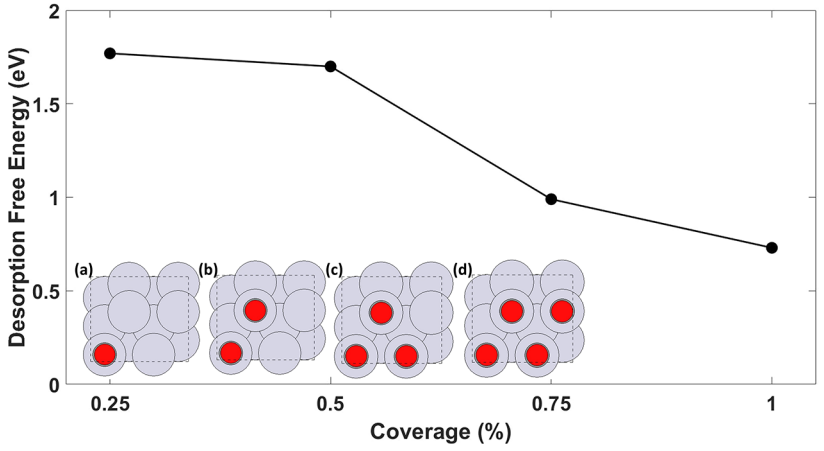

Figure 5. Desorption-free energies for CO(g) on a Pt(111) surface slab with increasing CO coverage. Inset images show CO coverage of (a) 25%, (b) 50%, (c) 75%, and (d) 100%.

cluster/Pt(111) interface, followed by migration of *CO to the Pt(111) microfacet. On the Pt(111) surface, the *CO intermediate is hydrogenated to *CHO and then to *CHOH, as shown in Figure 3. From here, the mechanism splits into two branches, one of which is the formation of $*CH_2OH$, followed by methanol desorption and the other being the formation of *CH + H_2O (g), $*CH_2$, and then $*CH_3$, followed by methane desorption (Figure 3). Compared with the Zr-cluster/Pt(111) model, forming methane over methanol is favorable on a Pt(111) surface. The activation free energy for methanol formation calculated from the lowest energy intermediate *CO is 2.1 eV. In comparison, the overall activation free energy for methane formation is referenced to the lowest energy intermediate of $*CH_3$ and is 1.5 eV.

Our calculations show that the CO migration from the Zr-cluster/Pt(111) model interface to the Pt(111) surface is feasible and reduces the activation energy to form methane from 3.27 eV at the interface to 1.5 eV when hydrogenation takes place on the Pt(111) slab. These results agree with our previous experiments, which indicate that the interface between cluster and Pt NP facilitates methane formation and that CO is an intermediate of this reaction.[13]

The formation of CO in UiO-67-Pt has previously been experimentally characterized using FT-IR.[12] It was observed that a signal at 2040 cm^{-1} (see the inset in Figure 4), which was assigned to Pt−CO, was increasing gradually as the reaction progressed. This signal could not be reproduced computationally by using a Pt(111) slab. However, studies on the Pt_{55} nanoparticle show that this CO signal at around 2030 cm^{-1} could be reproduced with varying CO coverages on its surface (see Figure 4). Our theoretical model also shows that the intensity increases as the CO coverage varies from 28 to 100%. With these results, we concluded that the edges of the Pt nanoparticle are responsible for the CO signal and that CO is a product of the CO_2 hydrogenation reaction at the interface of the Zr-cluster/Pt(111) model.

CO Formation. While studying CO_2 hydrogenation on the Pt(111) surface, we found that CO adsorbs very strongly on the platinum surface with desorption-free energy to the gas phase of 1.8 eV at low CO coverage. However, desorption-free energies are significantly decreased when the CO coverage

https://doi.org/10.1021/acscatal.3c03401
ACS Catal. 2024, 14, 382−394

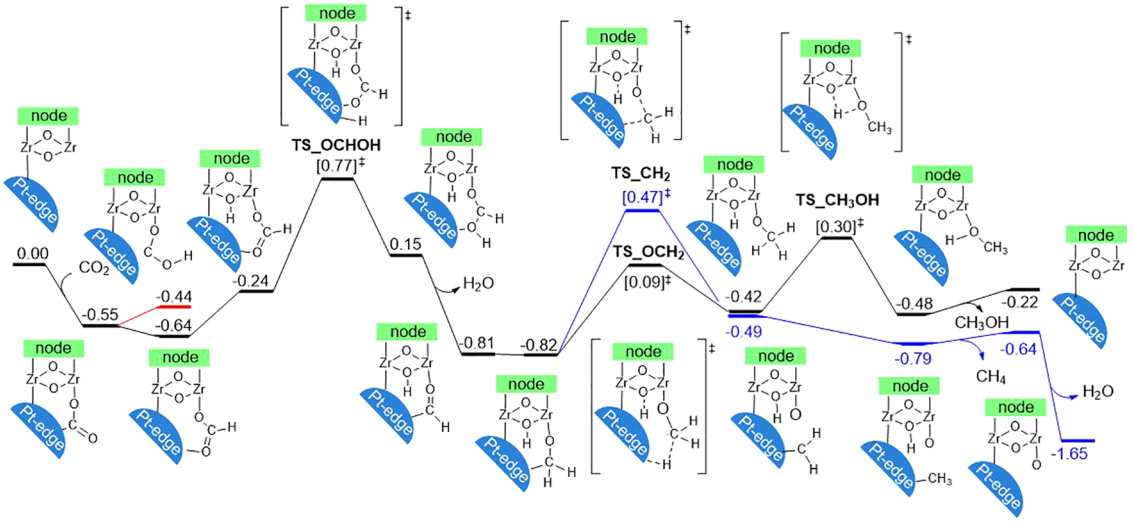

Figure 6. Calculated free energy (in eV) diagrams and energy barriers for CO_2 reduction reaction toward methane and methanol formation on Zr-cluster/Pt-edge model at 170 °C and 8 bar.

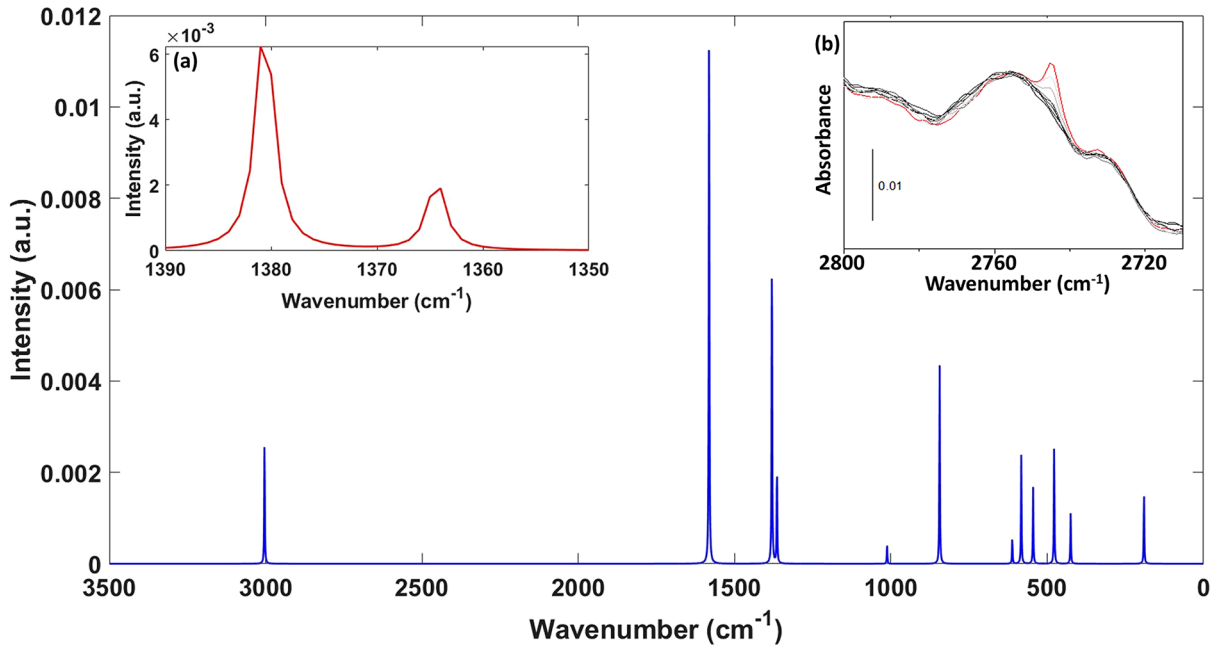

Figure 7. Simulated IR spectroscopy plot of bidentate formate intermediate at missing linker defect site (identical spectra were also observed on the Zr-cluster/Pt(111) and Zr-cluster/Pt-edge models). Inset (a) is a magnified version showing the ν_s(COO) and δ(CH) that combine to be seen as formate signals in the experiments.[13] Inset (b) shows the FT-IR spectra of bidentate formate on Zr-clusters.

increases, as shown in Figure 5. The desorption-free energy of CO at varying coverage was calculated using a periodic 2 × 2 platinum surface. These calculations show that as the CO coverage increases to 75%, the CO desorption-free energy is lowered to ∼1 eV, and at 100% CO coverage, it is further lowered to 0.7 eV. This high CO coverage is possible due to the strong adsorption energies and high pressure, consistent with the increasing Pt−CO IR signal observed in experiments.

$Zr_6O_4(OH)_4$ Cluster on a Platinum-Edged Surface (Zr-Cluster/Pt-Edge Model). The free energies obtained for the Zr-cluster/Pt-edge model differ significantly from those obtained with the Zr-cluster/Pt(111) model, as can be seen from the free energy diagram in Figure 6. The differences begin immediately with a CO_2 molecule being able to adsorb onto the defect site exothermically, followed by hydrogenation of the carbon to form *OCHO (formate) instead of *OCOH (carboxyl). In this case, formate (−0.1 eV) was found to be thermodynamically more favorable than *OCOH (0.1 eV), while in the Zr-cluster/Pt(111) model, *OCHO was less stable than *OCOH by 0.6 eV.

For the next step, unlike the Zr-cluster/Pt(111) model, we found that it is feasible to protonate the μ^3-O at the defect site on the $Zr_6O_4(OH)_4$ cluster, and this is preferred over carbon or oxygen hydrogenation of the *OCHO intermediate by 1.33 and 1.24 eV, respectively. The following step is the hydrogenation of *OCHO (formate) to form *OCHOH (formic acid). This step has a free energy barrier of 1.41 eV, taking formate (the lowest free energy intermediate) as the energy reference. Hydrogen transfer to the OH group of formic acid eliminates water and adsorbed formaldehyde

https://doi.org/10.1021/acscatal.3c03401
ACS Catal. 2024, 14, 382−394

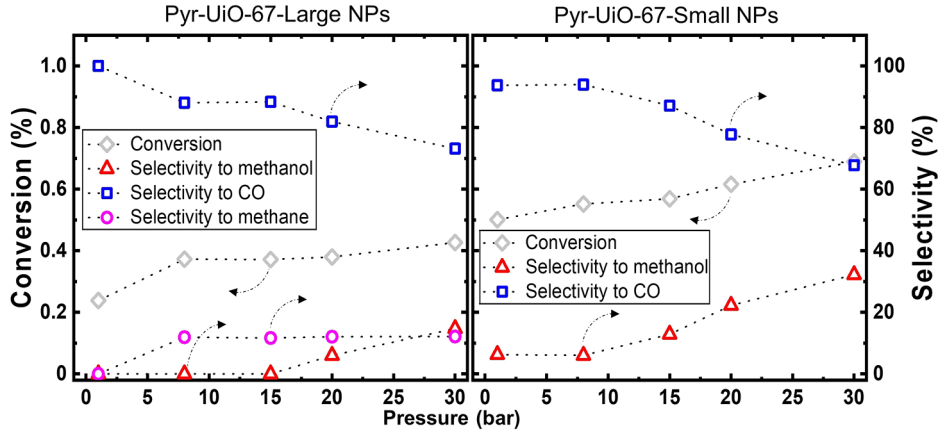

Figure 8. CO_2 conversion (left axis) and product selectivity (right axis) as a function of pressure (T = 170 °C) for Pyr-UiO-67-large NPs (left graph) and Pyr-UiO-67-small NPs (right graph). CO_2 conversion (diamond), methanol (triangle), CO (square), and methane (circle) selectivity. Conditions: CO_2/H_2/inert = 1/6/2, τ = 0.01 $g_{UiO\text{-}67\text{-}Pt}$ min mL^{-1}.

(*OCH), which is further hydrogenated to give *OCH_2 and then *OCH_3. Finally, the formation of adsorbed methanol from *OCH_3 occurs via hydrogen transfer from μ^3-OH to methoxy oxygen, which has a transition state of 1.12 eV above formate. The desorption of methanol is only slightly endergonic (0.26 eV).

Attempts to find a transition state for methane formation from the *OCH_3 intermediate in the Zr-cluster/Pt-edge model were unsuccessful and are discussed in Figure S12 of the SI. Similar to the Zr-cluster/Pt(111) model, further attempts to break the O−C bond at the *OCH_3 intermediate to migrate CH_3 onto the Pt-edge were unsuccessful (see Figure S12 of the SI). However, the O−C bond cleavage in the *OCH_2 intermediate forms the *CH_2 intermediate on the Pt-edge. This step has an energy barrier of 1.3 eV (Figures 6 and S5). The *CH_2 can then be hydrogenated to form *CH_3 and then desorbed as CH_4 by two consecutive hydrogen transfer reactions, one from the surface and one from μ^3-OH, as shown in Figure 6.

Overall, Figure 6 shows that the highest free energy barrier for CO_2 hydrogenation on the Zr-cluster/Pt-edge model is the hydrogenation of formate, which has a barrier of 1.41 eV. After this step, the formation of methanol is preferred over the formation of methane. This result is consistent with the experimental data showing that formate is an intermediate for methanol formation and the inverse KIE indicating a shift in hybridization in the rate-limiting step, from sp^2 in *OCHO to sp^3 in *OCH_2O as shown in Figure S19 of the SI.

We further reproduced the IR signal at 2745 cm^{-1} assigned experimentally to formate with formate obtained by using the computational models in Figure 1. This IR signal is a combination mode of ν_s(COO) + δ(CH) and can be obtained only if the two modes are present. The formate intermediate is thermodynamically favorable in our calculations during the CO_2 reduction mechanism in the missing linker defect site (Figure 1f) and the Zr-cluster/Pt-edge model (Figure 1c). In the case of the Zr-cluster/Pt-edge model, it was found at 2648 cm^{-1}, as shown in Figure S13 of the SI; we think that this shift is due to the stabilizing effect of the platinum surface on the ν_s(COO) mode. On the missing linker defect site and the formate linkers located at the top of the Zr-cluster and away from the Pt surface of the Zr-cluster/Pt-edge and Zr-cluster/Pt(111) models, the formate IR signal was observed at ∼2747 cm^{-1}, very close to the experimental value, as shown in Figure 7. It must be noted that for the formate linkers at the sides of the Zr-cluster and closer to the platinum terraces and edges, the ν_s(COO) signal was once again absent. To explain the experimental observations with these results, we should consider the flexibility of the Zr-cluster, in which formate can change its coordination from bidentate (κ^2) to monodentate (κ^1). This process could allow the formate intermediate generated at the interface to migrate to the top position, where κ^2 coordination is preferred. Similarly, formate could migrate back to the interface to be further hydrogenated.

Missing Linker Defect and Pt_{55} Nanoparticles. The good agreement between the experimental and simulated IR signals for the formate and CO intermediates in the missing linker defect and Pt_{55} nanoparticle models, respectively (Figure 1f,e), encouraged us to consider these models for the CO_2 hydrogenation reaction, despite their clear limitations. For the missing linker defect model, the thermodynamics for the CO_2 hydrogenation reaction is highly energetically unfavorable. All steps, including the CO_2 adsorption, are endergonic until the formation of the OCH, which has an energy of almost 3 eV (see Figure S14). This result suggests that the encapsulated Pt NP, besides providing hydrogen atoms, activates the reaction intermediates.

In the case of the Pt_{55} nanoparticle, as shown in Figure S15 of the SI, the adsorption of CO_2 is slightly favorable (−0.10 eV), and the following steps are highly exergonic until the formation of CO, which has an energy of −1.48 eV. Further hydrogenation of this intermediate is endergonic until the formation of CHOH intermediate at −0.49 eV. This high energy (0.99 eV) would limit the formation of both methanol and methane. However, a study by Li, Lin, and co-workers on the finite size effects of platinum metal clusters[39] shows unreasonably high adsorption energies in small metal clusters due to geometry and electronic finite size effect, which only vanishes when the platinum clusters are larger than 1.6 nm. In our case, the diameter of the Pt_{55} NP is 1.1 nm; therefore, the adsorption energies may be overestimated. Therefore, we did not further analyze the energies obtained by using this model.

Experimental Results with Pyrolyzed UiO-67-Pt (Pyr-UiO-67-Small and Large NPs Models). The computational results presented above suggest that the interface between the Zr-cluster and a flat Pt(111) surface favors a mechanism via a CO intermediate, which could be transformed to methanol at the interface or migrate to the Pt(111) surface to form

https://doi.org/10.1021/acscatal.3c03401
ACS Catal. 2024, 14, 382−394

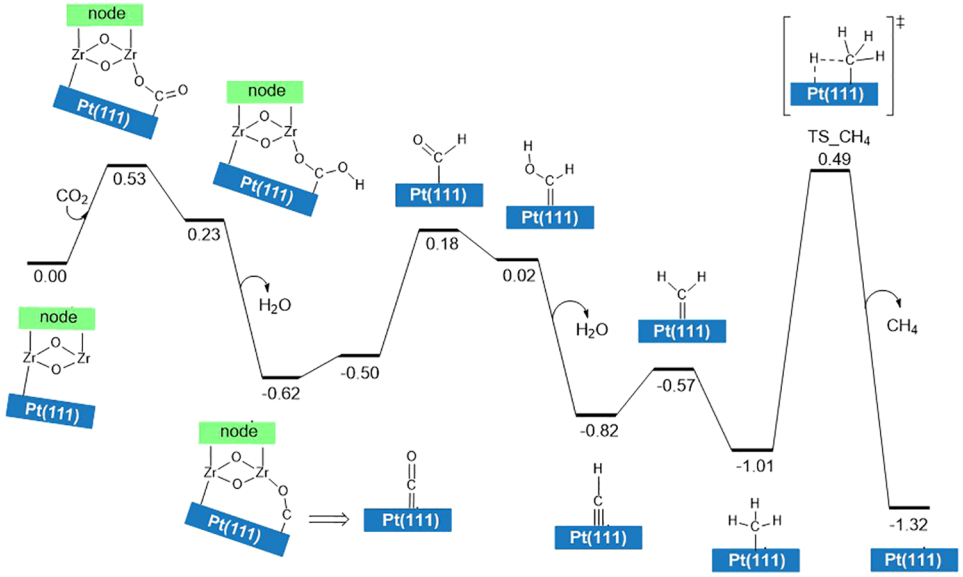

Figure 9. Free energy profile (in eV) along with a schematic representation of the proposed reaction mechanism of CO_2 hydrogenation to methane at the interface of the defective Zr-cluster/Pt(111) model, followed by migration of CO intermediates to the Pt(111) surface, where it is reduced further to methane.

methane. However, for the Zr-cluster on a platinum-edged surface, the reaction proceeds via a formate intermediate and is selective for methanol formation. To support these results and validate our computational models, we synthesized two new catalytic systems with different encapsulated nanoparticle sizes (large and small NPs). The specific surface area and size of the Pt NPs of the pyrolyzed catalysts, Pyr-UiO-67-large NPs, and Pyr-UiO-67-small NPs, are shown in Table S3. The Pt NPs in Pyr-UiO-67-large NPs have a most abundant size of 7.5 nm, while those in Pyr-UiO-67-small NPs have a most abundant size of 2.2 nm. The substantial difference in size is attributed to the order of sample pretreatments. NPs of mostly 6.5−8.5 nm (Pyr-UiO-67-large NPs) are formed by reducing the sample in H_2 before pyrolysis. The pyrolysis of the sample at 550 °C caused a severe collapse of the framework (Figures S23, S24 and Table S4). The size distribution of the Pt NPs for Pyr-UiO-67-large NPs (Figure S25) shows some NPs as large as 12.5 nm. Comparing this size with the NP size of UiO-67-Pt (8.5 nm, Figure S26) suggests that the pyrolysis step causes some NPs to sinter. For Pyr-UiO-67-small NPs, the sample was first pyrolyzed, which caused a similar framework collapse (Figure S24). It is believed that the reduced porosity of the sample hindered the growth of the Pt NPs during reduction, resulting in small NPs. As expected, the pyrolysis step caused a complete loss of crystallinity in the frameworks (Figure S27). For Pyr-UiO-67-large NPs, the Pt NPs are large enough to be detected as broad peaks in the diffractogram.

The conversion of CO_2 and the selectivity to methane, methanol, and CO for Pyr-UiO-67-large NPs and Pyr-UiO-67-small NPs are shown in Figures 8 and S29. As expected, the conversion of CO_2 for Pyr-UiO-67-large NPs is lower than for Pyr-UiO-67-small NPs due to the lower percentage of surface Pt atoms, effectively reducing the number of active sites as the interface between Pt and Zr is diminished. For the Pyr-UiO-67-large NPs catalyst, methane was detected at already 8 bar, but no methane could be detected for the Pyr-UiO-67-small NPs. The selectivity to methanol was larger under all conditions investigated for Pyr-UiO-67-small NPs.

DISCUSSION

We can assume that the catalyst sample with large nanoparticles (Pyr-UiO-67-large NPs) has a high abundance of flat surfaces, and therefore, the node/Pt interfaces could be described by the Zr-cluster/Pt(111) model. On the other hand, the catalyst sample with small nanoparticles (Pyr-UiO-67-small NPs) has relatively abundant edges that can be described by the Zr-cluster/Pt-edge at the interface. Using this approximation, our computational results can be used to propose a mechanism for the formation of methanol, methane, and CO in the UiO-67-Pt catalytic system that can explain many experimental observations.

A high activation energy for methane formation on the Zr-cluster/Pt(111) and Zr-cluster/Pt-edge models suggests that methane formation is not feasible at the interface sites. Indeed, reasonable energy barriers were only found when considering the C−O bond cleavage of the formaldehyde intermediate at the Zr-cluster/Pt interfaces, followed by CH_2 hydrogenation in the Pt surface. The activation energy is lowered by considering that CO formed at the Zr-cluster/Pt(111) interface migrates to the Pt(111) surface, where CO can be desorbed to the gas phase or reduced further to methane. With these results, we propose the methane formation mechanism shown in Figure 9, where the activation energy for methane formation, referenced to the lowest energy intermediate of $*CH_3$, is 1.5 eV (see Table 1). This mechanism is also supported by kinetic studies that suggest CO as a reaction intermediate and the observation of methane formation only on the catalyst sample with large nanoparticles, as shown in Figure 8. Our studies have also shown that CO is released from the Pt surfaces at high CO coverages when the CO desorption energy decreases to 1.0 eV or lower (Table 1). However, the CO adsorbed on Pt, experimentally observed by IR, is located at the Pt-edges and could be reproduced only on the Pt_{55} NP model with increasing CO coverage.

Similarly, a mechanism for methanol formation is suggested in Figure 10, which shows that the interface of a defective Zr-cluster and Pt NP is necessary for methanol formation.

https://doi.org/10.1021/acscatal.3c03401
ACS Catal. 2024, 14, 382−394

Table 1. Density Functional Theory (DFT) Calculated the Kinetic Barriers for Methane, Methanol, and CO Formation[a]

Model	Methane/eV	Methanol/eV	CO(g)/eV
Zr-cluster/Pt(111)	3.26	1.43	
Zr-cluster/Pt-edge	1.41 (1.3)	1.41 (1.1)	
Pt(111) surface	1.55	2.16	0.7−1.7

[a]The energies in parenthesis in the Zr-cluster/Pt-edge interface model are the highest calculated to form methane and methanol after the rate-limiting step, which is common for both products. CO(g) formation takes place at the (111) microfacet of Pt NPs, but the CO intermediates are formed from initial CO_2 reduction at the interface between the Zr-cluster and Pt(111) and diffuse to the microfacet. The interface between Zr-cluster and Pt-edges preferentially catalyzes formate formation instead of CO.

Methanol formation via a formate intermediate, as supported by the kinetic studies with H_2 and D_2,[13] was only observed on the Zr-cluster/Pt-edge model and not on the Zr-cluster/Pt(111) model. This result indicates that methanol is formed in a larger amount when Zr-clusters interact with the edges of the nanoparticle. Since this interaction with edges is possible on both large and small nanoparticles, methanol can be observed in both catalytic systems. However, the selectivity toward methanol is twice as large when small instead of large NPs are used, as shown in Figure 8. This is because, in the case of small nanoparticles, more edges are available to form Zr-cluster/Pt-edge interfaces. The activation free energy for methanol formation at the Zr-cluster/Pt-edge model, from the lowest energy intermediate *OCH_2, is 1.29 eV. However, the RDS for methanol formation is formate hydrogenation at 1.41 eV (see Table 1).

We could not assign the experimentally detected formate IR signal to the formate intermediate formed at the Zr-cluster/Pt-edge interface. However, a bidentate formate IR signal was observed on the Zr-clusters, where the formate capping agents point away from the Pt NP. This observation indicates the possibility of formate migration from the interface through the node via ligand exchange with other capping agents at the Zr node.

The activation energies for the formation of methanol and methane (Table 1) show that the most preferred pathway for methanol formation is at the Zr-cluster/Pt-edge interface, while methane is the preferred product at the Pt(111). Even though methane has a similar activation energy to methanol, only methane goes via CO formation and competes with CO desorption, which is the preferred product at high coverages. The latter result explains the methanol selectivity observed in the UiO-67-Pt catalytic system.

CONCLUSIONS

We have investigated different possible active sites within the UiO-67 MOF containing platinum nanoparticles and aimed to identify the most favorable pathway for CO_2 reduction toward methanol, methane, and CO formation. The reaction mechanism for this complex catalytic system can only be understood with the combination of calculations and experiments. Many experimental observations from previous studies could be described by the combination of three computational models: a $Zr_6O_4(OH)_4$ cluster on a platinum-edged surface, a $Zr_6O_4(OH)_4$ cluster on a Pt(111) surface, and an isolated Pt(111) surface. The interface model selection was based on adsorption energies of the $Zr_6O_4(OH)_4$ cluster with two capping agent defect sites on the Pt(111) surface and missing linker defect formation. The preferred orientation of the Zr-cluster toward the Pt surface is consistent with the Pt NP growing on the tetrahedral cage to increase its interaction with the linkers and the Zr-nodes.

We found that a synergistic interaction between defective $Zr_6O_4(OH)_4$ clusters and encapsulated nanoparticles is needed for favoring CO_2 activation. In the cases in which node defects are located on Pt-edges, methanol is the preferred product. We show that formate is an intermediate of this reaction, and its hydrogenation is the RDS. Migration of formate over the Zr node is feasible, slowing down its hydrogenation, and hence, it can be detected experimentally. When node defects are located on a Pt(111) surface, the formation of CO is preferred over that of formate, and this CO migrates over the Pt surface, favoring its hydrogenation to methane. CO desorption is favored at large CO coverages, and this desorption is the RDS for CO formation. This reactivity model is consistent with the methane formation observed when pyrolyzed UiO-67 featuring large Pt NPs is used and is also consistent with the selective formation of methanol over methane in the UiO-67-Pt and pyrolyzed UiO-67 with small Pt NPs characterized by a large number of Pt-edges.

This study shows that NPs encapsulated in MOFs are multicomponent systems that should be treated by considering multiple models. The migration of reaction intermediates among these models or components is key to account for the experimental observations. These results highlight the difficulties of having selective reactions using heterogeneous catalysts. On the other hand, the possibility of understanding the reaction mechanism allows for tuning the different sites to favor the desired reactions and prevent those undesired.

ASSOCIATED CONTENT

Supporting Information

The Supporting Information is available free of charge at https://pubs.acs.org/doi/10.1021/acscatal.3c03401.

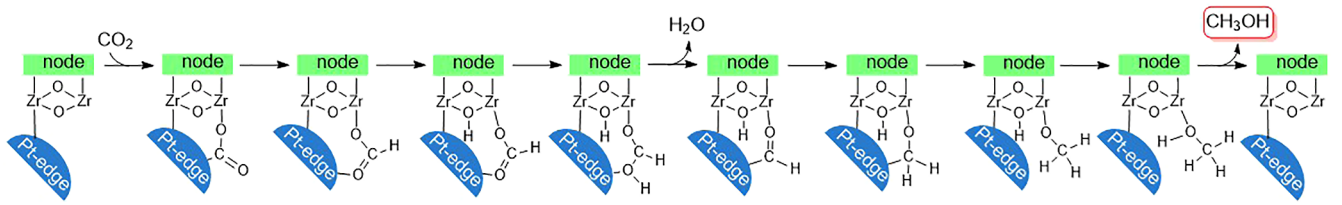

Figure 10. Schematic representation of the proposed reaction mechanism of CO_2 hydrogenation to methanol at a defective Zr-cluster/Pt-edge model.

https://doi.org/10.1021/acscatal.3c03401
ACS Catal. 2024, 14, 382−394

Details of DFT calculations, experimental procedures, and characterization results (PDF)

Coordinates of all of the intermediates and transition states used in DFT calculations (XYZ)

AUTHOR INFORMATION

Corresponding Authors

Unni Olsbye − *Centre for Materials Science and Nanotechnology, Department of Chemistry, University of Oslo, N-0315 Oslo, Norway;* orcid.org/0000-0003-3693-2857; Email: unni.olsbye@kjemi.uio.no

Ainara Nova − *Centre for Materials Science and Nanotechnology, Department of Chemistry, University of Oslo, N-0315 Oslo, Norway; Hylleraas Centre for Quantum Molecular Sciences, Department of Chemistry, University of Oslo, N-0315 Oslo, Norway;* orcid.org/0000-0003-3368-7702; Email: ainara.nova@kjemi.uio.no

Egill Skúlason − *Science Institute and Faculty of Industrial Engineering, Mechanical Engineering and Computer Science, University of Iceland, 107 Reykjavík, Iceland;* orcid.org/0000-0002-0724-680X; Email: egillsk@hi.is

Authors

Sri Harsha Pulumati − *Science Institute and Faculty of Industrial Engineering, Mechanical Engineering and Computer Science, University of Iceland, 107 Reykjavík, Iceland;* orcid.org/0009-0001-6287-7620

Dag Kristian Sannes − *Centre for Materials Science and Nanotechnology, Department of Chemistry, University of Oslo, N-0315 Oslo, Norway*

Christia R. Jabbour − *Inorganic Chemistry and Catalysis, Institute for Sustainable and Circular Chemistry and Debye Institute for Nanomaterials Science, Utrecht University, 3584 CG Utrecht, The Netherlands*

Laurens D. B. Mandemaker − *Inorganic Chemistry and Catalysis, Institute for Sustainable and Circular Chemistry and Debye Institute for Nanomaterials Science, Utrecht University, 3584 CG Utrecht, The Netherlands*

Bert M. Weckhuysen − *Inorganic Chemistry and Catalysis, Institute for Sustainable and Circular Chemistry and Debye Institute for Nanomaterials Science, Utrecht University, 3584 CG Utrecht, The Netherlands;* orcid.org/0000-0001-5245-1426

Complete contact information is available at: https://pubs.acs.org/10.1021/acscatal.3c03401

Notes

The authors declare no competing financial interest.

ACKNOWLEDGMENTS

S.H.P., E.S., and A.N. acknowledge support by the "Nordic Consortium for CO_2 Conversion" NordForsk Project No. 85378, site.uit.no/nordco2 and the Norwegian Metacenter for Computational Science (NOTUR) for computational resources (Project No. nn4654k). S.H.P. and E.S. acknowledge support from the Icelandic Research Fund (Grant Nos. 196437-051 and 207283-051). A.N. acknowledges the support from the Research Council of Norway (FRINATEK Grant No. 250044 and Center of Excellence Grant No. 262695). D.K.S and U.O acknowledge the Research Council of Norway for financial support (Grant No. 288331 CO2LO).

REFERENCES

(1) Solomon, S.; Plattner, G.-K.; Knutti, R.; Friedlingstein, P. Irreversible climate change due to carbon dioxide emissions. *Proc. Natl. Acad. Sci. U.S.A.* **2009**, *106* (6), 1704−1709.

(2) Yuan, Y.; Qi, L.; Guo, T.; Hu, X.; He, Y.; Guo, Q. A review on the development of catalysts and technologies of CO2 hydrogenation to produce methanol. *Chem. Eng. Commun.* **2022**, *210*, 1791−1821.

(3) Jiang, X.; Nie, X.; Guo, X.; Song, C.; Chen, J. G. Recent advances in carbon dioxide hydrogenation to methanol via heterogeneous catalysis. *Chem. Rev.* **2020**, *120* (15), 7984−8034.

(4) Kattel, S.; Liu, P.; Chen, J. G. Tuning selectivity of CO2 hydrogenation reactions at the metal/oxide interface. *J. Am. Chem. Soc.* **2017**, *139* (29), 9739−9754.

(5) Li, K.; Chen, J. G. CO2 hydrogenation to methanol over ZrO2-containing catalysts: insights into ZrO2 induced synergy. *ACS Catal.* **2019**, *9* (9), 7840−7861.

(6) Meunier, F. C. Mixing copper nanoparticles and ZnO nanocrystals: A route towards understanding the hydrogenation of CO2 to methanol? *Angew. Chem., Int. Ed.* **2011**, *50* (18), 4053−4054.

(7) Lam, E.; Larmier, K.; Tada, S.; Wolf, P.; Safonova, O. V.; Copéret, C. Zr (IV) surface sites determine CH3OH formation rate on Cu/ZrO2/SiO2-CO2 hydrogenation catalysts. *Chin. J. Catal.* **2019**, *40* (11), 1741−1748.

(8) Larmier, K.; Liao, W. C.; Tada, S.; Lam, E.; Verel, R.; Bansode, A.; Urakawa, A.; Comas-Vives, A.; Copéret, C. CO2-to-methanol hydrogenation on zirconia-supported copper nanoparticles: reaction intermediates and the role of the metal−support interface. *Angew. Chem., Int. Ed.* **2017**, *56* (9), 2318−2323.

(9) Lam, E.; Larmier, K.; Wolf, P.; Tada, S.; Safonova, O. V.; Copéret, C. Isolated Zr surface sites on silica promote hydrogenation of CO2 to CH3OH in supported Cu catalysts. *J. Am. Chem. Soc.* **2018**, *140* (33), 10530−10535.

(10) Wesselbaum, S.; Moha, V.; Meuresch, M.; Brosinski, S.; Thenert, K. M.; Kothe, J.; Vom Stein, T.; Englert, U.; Hölscher, M.; Klankermayer, J.; Leitner, W. Hydrogenation of carbon dioxide to methanol using a homogeneous ruthenium−Triphos catalyst: from mechanistic investigations to multiphase catalysis. *Chem. Sci.* **2015**, *6* (1), 693−704.

(11) Lane, E. M.; Zhang, Y.; Hazari, N.; Bernskoetter, W. H. Sequential hydrogenation of CO2 to methanol using a pincer iron catalyst. *Organometallics* **2019**, *38* (15), 3084−3091.

(12) Gutterød, E. S.; Øien-Ødegaard, S.; Bossers, K.; Nieuwelink, A.-E.; Manzoli, M.; Braglia, L.; Lazzarini, A.; Borfecchia, E.; Ahmadigoltapeh, S.; Bouchevreau, B.; et al. CO2 Hydrogenation over Pt-Containing UiO-67 Zr-MOFs— The Base Case. *Ind. Eng. Chem. Res.* **2017**, *56* (45), 13206−13218.

(13) Gutterød, E. S.; Lazzarini, A.; Fjermestad, T.; Kaur, G.; Manzoli, M.; Bordiga, S.; Svelle, S.; Lillerud, K. P.; Skúlason, E.; Øien-Ødegaard, S.; Nova, A.; Olsbye, U. Hydrogenation of CO2 to Methanol by Pt Nanoparticles Encapsulated in UiO-67: Deciphering the Role of the Metal−Organic Framework. *J. Am. Chem. Soc.* **2020**, *142* (2), 999−1009.

(14) Gutterød, E. S.; Pulumati, S. H.; Kaur, G.; Lazzarini, A.; Solemsli, B. G.; Gunnæs, A. E.; Ahoba-Sam, C.; Kalyva, M. E.; Sannes, J. A.; Svelle, S.; Skúlason, E.; Nova, A.; Olsbye, U. Influence of Defects and H2O on the Hydrogenation of CO2 to Methanol over Pt Nanoparticles in UiO-67 Metal−Organic Framework. *J. Am. Chem. Soc.* **2020**, *142* (40), 17105−17118.

(15) Yuan, S.; Feng, L.; Wang, K.; Pang, J.; Bosch, M.; Lollar, C.; Sun, Y.; Qin, J.; Yang, X.; Zhang, P. Stable metal−organic frameworks: design, synthesis, and applications. *Adv. Mater.* **2018**, *30* (37), No. 1704303.

(16) Valenzano, L.; Civalleri, B.; Chavan, S.; Bordiga, S.; Nilsen, M. H.; Jakobsen, S.; Lillerud, K. P.; Lamberti, C. Disclosing the complex structure of UiO-66 metal organic framework: a synergic combination of experiment and theory. *Chem. Mater.* **2011**, *23* (7), 1700−1718.

(17) Cavka, J. H.; Jakobsen, S.; Olsbye, U.; Guillou, N.; Lamberti, C.; Bordiga, S.; Lillerud, K. P. A new zirconium inorganic building

brick forming metal organic frameworks with exceptional stability. *J. Am. Chem. Soc.* **2008**, *130* (42), 13850−13851.
(18) Wu, H.; Chua, Y. S.; Krungleviciute, V.; Tyagi, M.; Chen, P.; Yildirim, T.; Zhou, W. Unusual and highly tunable missing-linker defects in zirconium metal−organic framework UiO-66 and their important effects on gas adsorption. *J. Am. Chem. Soc.* **2013**, *135* (28), 10525−10532.
(19) Zhu, Y.; Zheng, J.; Ye, J.; Cui, Y.; Koh, K.; Kovarik, L.; Camaioni, D. M.; Fulton, J. L.; Truhlar, D. G.; Neurock, M.; et al. Copper-zirconia interfaces in UiO-66 enable selective catalytic hydrogenation of CO2 to methanol. *Nat. Commun.* **2020**, *11* (1), No. 5849.
(20) Rungtaweevoranit, B.; Baek, J.; Araujo, J. R.; Archanjo, B. S.; Choi, K. M.; Yaghi, O. M.; Somorjai, G. A. Copper nanocrystals encapsulated in Zr-based metal−organic frameworks for highly selective CO2 hydrogenation to methanol. *Nano Lett.* **2016**, *16* (12), 7645−7649.
(21) Zhang, J.; An, B.; Li, Z.; Cao, Y.; Dai, Y.; Wang, W.; Zeng, L.; Lin, W.; Wang, C. Neighboring Zn−Zr sites in a metal−organic framework for CO2 hydrogenation. *J. Am. Chem. Soc.* **2021**, *143* (23), 8829−8837.
(22) Lippert, B. G.; Parrinello, J. H.; Michele. A hybrid Gaussian and plane wave density functional scheme. *Mol. Phys.* **1997**, *92* (3), 477−488, DOI: 10.1080/00268979709482119.
(23) VandeVondele, J.; Krack, M.; Mohamed, F.; Parrinello, M.; Chassaing, T.; Hutter, J. Quickstep: Fast and accurate density functional calculations using a mixed Gaussian and plane waves approach. *Comput. Phys. Commun.* **2005**, *167* (2), 103−128.
(24) Perdew, J. P.; Burke, K.; Ernzerhof, M. Generalized Gradient Approximation Made Simple. *Phys. Rev. Lett.* **1996**, *77* (18), 3865−3868.
(25) Goedecker, S.; Teter, M.; Hutter, J. Separable dual-space Gaussian pseudopotentials. *Phys. Rev. B: Condens. Matter Mater. Phys.* **1996**, *54* (3), 1703−1710.
(26) Hartwigsen, C.; Goedecker, S.; Hutter, J. Relativistic separable dual-space Gaussian pseudopotentials from H to Rn. *Phys. Rev. B: Condens. Matter Mater. Phys.* **1998**, *58* (7), 3641.
(27) Grimme, S.; Ehrlich, S.; Goerigk, L. Effect of the damping function in dispersion corrected density functional theory. *J. Comput. Chem.* **2011**, *32* (7), 1456−1465.
(28) Grimme, S.; Antony, J.; Ehrlich, S.; Krieg, H. A consistent and accurate ab initio parametrization of density functional dispersion correction (DFT-D) for the 94 elements H-Pu. *J. Chem. Phys.* **2010**, *132* (15), No. 154104.
(29) Lu, T.; Chen, Q. Shermo: A general code for calculating molecular thermochemistry properties. *Comput. Theor. Chem.* **2021**, *1200*, No. 113249.
(30) Henkelman, G.; Jónsson, H. Improved tangent estimate in the nudged elastic band method for finding minimum energy paths and saddle points. *J. Chem. Phys.* **2000**, *113* (22), 9978−9985.
(31) Henkelman, G.; Uberuaga, B. P.; Jónsson, H. A climbing image nudged elastic band method for finding saddle points and minimum energy paths. *J. Chem. Phys.* **2000**, *113* (22), 9901−9904.
(32) Sannes, D. K.; Øien-Ødegaard, S.; Aunan, E.; Nova, A.; Olsbye, U. Quantification of Linker Defects in UiO-Type Metal−Organic Frameworks. *Chem. Mater.* **2023**, *35*, 3793−3800, DOI: 10.1021/acs.chemmater.2c03744.
(33) Skúlason, E.; Faraj, A. A.; Kristinsdóttir, L.; Hussain, J.; Garden, A. L.; Jónsson, H. Catalytic activity of Pt nano-particles for H 2 formation. *Top. Catal.* **2014**, *57*, 273−281.
(34) Casey-Stevens, C. A.; Lambie, S. G.; Ruffman, C.; Skúlason, E.; Garden, A. L. Geometric and electronic effects contributing to N2 dissociation barriers on a range of active sites on Ru nanoparticles. *J. Phys. Chem. C* **2019**, *123* (50), 30458−30466.
(35) Kokalj, A.; Causà, M. Periodic density functional theory study of Pt (111): surface features of slabs of different thicknesses. *J. Phys.: Condens. Matter* **1999**, *11* (39), 7463.
(36) Kokalj, A.; Lesar, A.; Hodošček, M.; Causa, M. Periodic DFT study of the Pt (111): A p (1× 1) atomic oxygen interaction with the surface. *J. Phys. Chem. B* **1999**, *103* (34), 7222−7232.
(37) Peterson, G. W.; Moon, S.-Y.; Wagner, G. W.; Hall, M. G.; DeCoste, J. B.; Hupp, J. T.; Farha, O. K. Tailoring the pore size and functionality of UiO-type metal−organic frameworks for optimal nerve agent destruction. *Inorg. Chem.* **2015**, *54* (20), 9684−9686.
(38) Katz, M. J.; Brown, Z. J.; Colón, Y. J.; Siu, P. W.; Scheidt, K. A.; Snurr, R. Q.; Hupp, J. T.; Farha, O. K. A facile synthesis of UiO-66, UiO-67 and their derivatives. *Chem. Commun.* **2013**, *49* (82), 9449−9451.
(39) Li, L.; Larsen, A. H.; Romero, N. A.; Morozov, V. A.; Glinsvad, C.; Abild-Pedersen, F.; Greeley, J.; Jacobsen, K. W.; Nørskov, J. K. Investigation of catalytic finite-size-effects of platinum metal clusters. *J. Phys. Chem. Lett.* **2013**, *4* (1), 222−226.

https://doi.org/10.1021/acscatal.3c03401
ACS Catal. 2024, 14, 382−394